



Trevisan, A., Venema, V., Kollet, S., & Rahman, A. S. M. M. (2020). The topographic control on land surface energy fluxes: a statistical approach to bias correction in *Journal of Hydrology*. *Journal of Hydrology*, 584, [124669].
<https://doi.org/10.1016/j.jhydrol.2020.124669>

Peer reviewed version

License (if available):
CC BY-NC-ND

Link to published version (if available):
[10.1016/j.jhydrol.2020.124669](https://doi.org/10.1016/j.jhydrol.2020.124669)

[Link to publication record in Explore Bristol Research](#)
PDF-document

This is the author accepted manuscript (AAM). The final published version (version of record) is available online via Elsevier at <https://www.sciencedirect.com/science/article/pii/S0022169420301293?via%3Dihub>. Please refer to any applicable terms of use of the publisher.

University of Bristol - Explore Bristol Research

General rights

This document is made available in accordance with publisher policies. Please cite only the published version using the reference above. Full terms of use are available:
<http://www.bristol.ac.uk/red/research-policy/pure/user-guides/ebr-terms/>

1 The topographic control on land surface energy
2 fluxes

3 Alessandra Trevisan^{a, *}, Victor Venema^a, Stefan Kollet^{b, c}, Mostaquimur Rahman^{a, ^I}

4 ^a Meteorological Institute, University of Bonn, Germany

5 ^b Agrosphere Institute, Research Centre Juelich, Germany

6 ^c Centre for High-Performance Scientific Computing in Terrestrial System,
7 Geoverbund, ABC/J, Germany

8 ^I present address: Department of Civil Engineering, University of Bristol, UK

9 ^{*}Corresponding Author: A. Trevisan, trevisan@uni-bonn.de

10

11 **Abstract**

12 Subsurface hydrodynamics are an important component of the hydrological cycle
13 and a key factor in the partitioning of the land surface energy fluxes. Because
14 also of computational reasons they are often neglected, or strongly simplified, in
15 numerical weather prediction and climate models. Particularly in regions where
16 the water table is shallow, soil moisture acts as a link between land, atmosphere
17 and groundwater and, because of its long-term memory represents a buffer for
18 the effects of climate variability. To dynamically model this system we couple
19 a variably saturated groundwater flow model (ParFlow) with a surface model
20 (CLM). In order to overcome the computational limitations of such an explicit
21 representation of the groundwater dynamics, we propose an approach for the
22 statistical correction of the bias of the energy fluxes of a simple scheme, based
23 on the comparisons with fully-coupled subsurface-land-atmosphere simulations.
24 This simple dynamical scheme computes the potential latent heat flux in case
25 of near saturation. In particular, we focus on the ability of topography-related
26 indices, such as the topographic wetness index and the depth-to-water index,
27 to provide information on the availability of water for evapotranspiration. The
28 topographic indices confirm to be good predictors for the moisture availability.
29 While the small scale structure cannot be captured well, the results show that
30 the large-scale biases of latent heat flux over the domain are effectively removed.
31 Moreover, the bias corrected fluxes more accurately reproduce the fluxes of the
32 full modelling system than common used free drainage simulations. Thus, the
33 proposed approach can be useful in approximating the effect of groundwater on
34 land surface water and energy fluxes in e.g. regional climate models.

35 1 Introduction

36 Groundwater is the primary source of fresh water (*Gleick*, 1993) and a major
37 source of water supply for consumption, agriculture and industry. As an im-
38 portant element of the hydrologic cycle, groundwater sustains surface waters,
39 ecosystems and the aquatic communities that populate these areas (*Alley et al.*,
40 2002, *Fan and Miguez-Macho*, 2010). In the areas where soil moisture is the lim-
41 iting factor for the evapotranspiration, capillary rise from the groundwater table
42 may result directly into enhanced evapotranspiration (*Anyah et al.*, 2008) and
43 decreased infiltration (*Yeh and Eltahan*, 2005a). The water table depth (*wtd*) is a
44 function of groundwater dynamics and surface fluxes, such as evapotranspiration
45 and infiltration in the unsaturated zone (*York et al.*, 2002) and affects the soil
46 moisture profile at different space and time scales (*Vergnes et al.*, 2012). This is
47 reflected in the partitioning between surface and subsurface soil water and the
48 partitioning between surface sensible and latent heat fluxes, which affects the
49 terrestrial water and energy balance and the atmospheric processes (*Choi and*
50 *Liang*, 2010, *Leung et al.*, 2011).

51 The influence of groundwater storage on the energy and water exchanges
52 between soil and atmosphere can be conceptually understood for an idealized
53 hillslope. The hillslope is assumed to be divided into three regions with deep
54 (*C*), intermediate (*B*) and shallow (*A*) groundwater table (*Kollet and Maxwell*,
55 2008). Assuming that the water table follows the topography (a simplification
56 that is generally true for topographically driven groundwater flow), it is deeper
57 for the hill tops and shallower in the valleys, thus the three zones correspond
58 to three conceptual soil columns, that are connected by lateral groundwater
59 flow. In case *A*, where the water reaches or is close to the surface, the surface
60 processes are not water limited and small variations in water table depth do not
61 affect the land surface processes. In case *C*, the water can only drain downwards

62 (groundwater recharge) and there is no significant linkage between water table
 63 depth and land surface processes. Finally, in case *B*, which corresponds to the
 64 transition between the two regimes, the groundwater is at a “critical depth”, i.e.
 65 small changes in depth can alter the water availability for evaporation and root
 66 water uptake, allowing the vertical redistribution of soil moisture. This implies
 67 that in case *B*, there is a connection between groundwater and land surface
 68 related to the location of the water table and, thus, to the availability of water,
 69 which affects the energy fluxes (in particular the partition of energy between
 70 sensible and latent heat). In this regime it is therefore most important to model
 71 the position of the groundwater table and its evolution over time accurately.

72 This subdivision in three regimes was reflected in the relationship between
 73 latent heat and depth to groundwater found in simulations (*Soylu et al.*, 2011,
 74 *Kollet and Maxwell*, 2008) and was also confirmed in measured data (*Szilagyi*
 75 *et al.*, 2013). They show nearly no dependence of the fluxes on *wtd* for deep and
 76 shallow water tables (case *A* and case *C*), while for the intermediate region (case
 77 *B*) the curve is steep, implying that small changes in groundwater table influence
 78 the energy fluxes. The depth of this critical zone is also determined by the plant
 79 rooting depth (*Fan*, 2015). While this relationship between energy fluxes and
 80 water table depth is generally present in the critical zone, its strength can vary,
 81 depending on the soil composition and the land use type (*Maxwell et al.*, 2007,
 82 *Kollet and Maxwell*, 2008).

83 Despite the importance of groundwater dynamics for climate, the subsurface
 84 in *LSMs* is commonly represented by single soil columns. Moreover, a free
 85 drainage boundary condition at the bottom of the column is often used, which
 86 implies a negligible upward diffusive flux (*Yeh and Eltahan*, 2005b), even for
 87 regions of the domain where the water table is shallow in reality. This means
 88 that the lateral movement of water between the columns is neglected and water

is lost, instead of being laterally distributed towards the neighbouring columns, causing a bias in the mass and energy balance (*Tian et al.*, 2012, *Miguez-Macho et al.*, 2007).

In the last decades a number of studies, which are briefly reviewed below, demonstrated the importance of subsurface hydrodynamics for climate and weather modelling. The Land Surface Models (*LSMs*) provide the lower boundary condition for temperature and moisture in the General Circulation Models (*GCMs*), the mesoscale Regional Climate Models (*RCMs*) and the Numerical Weather Prediction models (*NWPs*). They describe the water and energy fluxes on the land surface, and the partitioning of the incoming precipitation into surface and subsurface runoff, evapotranspiration (*ET*) and soil moisture variation, but their description of the subsurface hydrodynamics is often highly simplified (*Tian et al.*, 2012). Several studies on the coupling of a groundwater component in *LSMs* showed that the inclusion of a dynamical representation of water table modifies the vertical profile of soil moisture and improves the water budget simulation (e.g., *York et al.*, 2002, *Maxwell and Miller*, 2005, *Jiang et al.*, 2009, *Lo and Famiglietti*, 2011, *Leung et al.*, 2011). Over short time scales and at the catchment scale, *Maxwell et al.* (2007) showed that a more realistic soil moisture distribution is obtained with the inclusion of the groundwater and that this affects the local atmospheric convection. *Miguez-Macho et al.* (2007) showed that the presence of the water table as the lower boundary of the soil causes a slower vertical drainage, that concurs with the upward capillary flux and the lateral groundwater convergence to the increase of soil moisture in the root zone, compared to a free-drainage run. In areas where the water table is deep, variations in land surface energy fluxes mostly depend on the precipitation (*Maxwell and Kollet*, 2008) and the free (gravity) drainage assumption is reasonable, since the saturated and unsaturated zones of the subsurface are not

116 interacting (*Vergnes et al.*, 2014, *Lo and Famiglietti*, 2010). When the water
 117 table is shallow, which is the case for almost 50% of the global land accord-
 118 ing to simulations (*Koirala et al.*, 2014), the upward flux from the aquifer to
 119 the shallow soil compartment and the decrease in infiltration (*Yeh and Eltahan*,
 120 2005b) affect the seasonal precipitation and temperature (*Jiang et al.*, 2009,
 121 *Anyah et al.*, 2008, *Maxwell and Kollet*, 2008, *Betts*, 2004).

122 In a study on the strength of the interactions between land and atmo-
 123 sphere, *Lo and Famiglietti* (2011) found that the effect of the groundwater on
 124 precipitation varies globally. In areas where the subsurface and atmosphere
 125 are strongly coupled, the groundwater presence enhances shallow soil moisture,
 126 which is transported vertically via evapotranspiration, impacting the initiation
 127 of convection. The augmented precipitation induces a positive feedback, where
 128 the wetter soil produces more evapotranspiration. Therefore, wet areas may get
 129 wetter and arid regions may get drier (*Chou and Neelin*, 2004). In reality, this
 130 rule of thumb for the expected trend in climate change is, however, extremely
 131 reductive and evidence of the opposite trend has been found, especially on land
 132 surfaces (*Greve et al.*, 2014).

133 In a comparison of two runs of a regional model with and without aquifer over
 134 a catchment in northeastern Kansas, *York et al.* (2002) found that between 5%
 135 and 20% (for wet and dry years, respectively) of ET comes from the aquifer. In
 136 a similar fashion, *Niu et al.* (2007) compared two experiments with free drainage
 137 and groundwater recharge as lower boundary condition, finding that the latter
 138 produces 4% to 16% (depending on the region) more annual evapotranspiration,
 139 with the transitional arid-to-wet areas presenting the largest effect of wetter soil
 140 on ET . Especially during dry periods, a shallow water table can sustain ET and
 141 reduce the sensitivity of surface soil moisture to precipitation anomalies (*Vergnes*
 142 *et al.*, 2014, *Yeh and Eltahan*, 2005a). Conversely, in areas with deeper ground-

143 water table the soil moisture is more sensitive to anomalies in precipitation,
144 which result in stronger fluctuations in the evaporative fraction (*Leung et al.*,
145 2011).

146 The variations in the fluxes of energy and moisture affect precipitation (*Anyah*
147 *et al.*, 2008) directly through convection or indirectly through advection, en-
148 creasing the spatial scale of the influence of groundwater on the atmosphere (*Yuan*
149 *et al.*, 2008). According to *Lam et al.* (2011), groundwater can locally contribute
150 more than 30% of evaporation in summer and increase the multi-year memory
151 of climate models, by a sustained influence of wet episodes for several years.
152 The water table acts as a buffer for the temporal variations of the soil moisture,
153 due to its slow changing nature (*Miguez-Macho et al.*, 2007, *York et al.*, 2002)
154 and reduces the impact of drought in forested regions (*Decker et al.*, 2013).
155 As the atmospheric forcing propagates through the land surface hydrologic cy-
156 cle, its anomalies persist in the water table levels, due to the longer memory
157 of groundwater compared to soil moisture; they are then transported upward
158 and impact the future climate (*Yeh and Eltahir*, 2005a). The ability of the
159 land surface to respond to anomalies in the climate is obviously affected by
160 land use change (*Leung et al.*, 2011) and the water table position responds also
161 to the depletion caused by groundwater pumping (*Leng et al.*, 2014), so the
162 anthropogenic influence alters significantly the hydrologic cycle (*Ferguson and*
163 *Maxwell*, 2010).

164 As discussed above, groundwater hydrodynamics are a key factor in influenc-
165 ing the energy fluxes at the land surface, yet a full three-dimensional subsurface
166 representation is computationally not feasible in global climate simulations. To
167 overcome this limitation we propose a Model Complexity Reduction Approach
168 (*MCRA*), connecting a parameterized groundwater representation for large scale
169 models, with small-scale physics based simulations. In the MCRA most of the

170 surface physics is modelled by a dynamical model and bias-corrected with a
 171 simple statistical model. The reverse approach was used for fast and accurate
 172 modelling radiative transfer in atmospheric models (*Venema et al.*, 2007; *Man-*
 173 *ners et al.*, 2009; *Schomburg et al.*, 2012). In these radiative transfer schemes,
 174 the simpler physical or statistical model was responsible for efficiently modelling
 175 the small-scale variability, while the complex physical model was used to reduce
 176 biases.

177 The approach is based on two sets of simulations. A full-physics simulation,
 178 *CplxRun*, represents the virtual reality, while a highly parameterized simulation,
 179 *LandParm*, is used as a reference. For this study, a Potential Latent Heat Run
 180 (*PotLERun*) is used as parameterized simulation. In it, the water table depth
 181 is fixed at the soil surface, as opposed to the *CplxRun*, where the water table is
 182 free to move in response to atmospheric forcing and topographic characteristics.

183 Topographic indices, such as Depth-To-Water and Topographic Index, ef-
 184 fectively represent the relative abundance of water at different locations in the
 185 watershed. Based on the fact that evapotranspiration is constrained by the
 186 availability of water and radiation, we will develop a statistical model for the
 187 correction of the *PotLERun*, in order to approximate the results of the *CplxRun*.
 188 The validity of the concept and the ability to correct the latent heat flux will
 189 be demonstrated using cross-validation in space.

190 The paper is structured as follows: in the first part we present the method-
 191 ology. The Model Complexity Reduction Approach is described as a general
 192 concept, followed by the simulations that this work is based on are then il-
 193 lustrated, starting with the model used to perform them. In section 2.4 the
 194 topographic indices used in the bias correction are presented and the sensitiv-
 195 ity of the latent heat flux to these indices and to other static parameters is
 196 shown. Finally, the statistical bias-correction model is explained, tested in a

197 cross-validation and compared to a free drainage simulation.

198 2 Methodology

199 In this section, we present the Model Complexity Reduction Approach, the
200 adaptive parameterization that is the core of this work. We then introduce the
201 simulation data, starting from the numerical model used to obtain them (Sec-
202 tion 2.2). The general characteristics of the domain are presented in Section 2.3,
203 with a particular focus on possible key parameters for a statistical model for
204 energy and moisture fluxes. The data originate from a previous study, *Rahman*
205 *et al.* (2014), where more details can be found.

206 2.1 Model Complexity Reduction Approach, MCRA

207 A Model Complexity Reduction Approach (*MCRA*) is proposed (Figure 1),
208 where a fast simplified model (*LandParm*) is run over the whole domain. Be-
209 cause of the simplifications, LandFast is biased. These biases are corrected
210 statistically (bias corrector). The biases are estimated by comparing LandFast
211 output to the results of a full complex model system (*LandCplx*) simulations.
212 In the *Updater* all the information is collected and elaborated, in order to provide
213 the updated values of spatially averaged latent heat, serving as lower boundary
214 flux for *GCMs* and *RCMs*. The information is represented by static parameters
215 used as predictors and the results of the full complex model system (*Landcplx*)
216 simulations.

217 In this study the *MCRA* adaptive approach is implemented using a LandFast
218 simulation where the water table was fixed at the surface and the source/sink
219 term turned off, to simulate a full availability of moisture (Potential Latent Heat
220 Run, *PotLERun*), while the rest of the setup (e.g., resolution) is identical to the
221 Complex Run. Because the soil is saturated, the computationally expensive

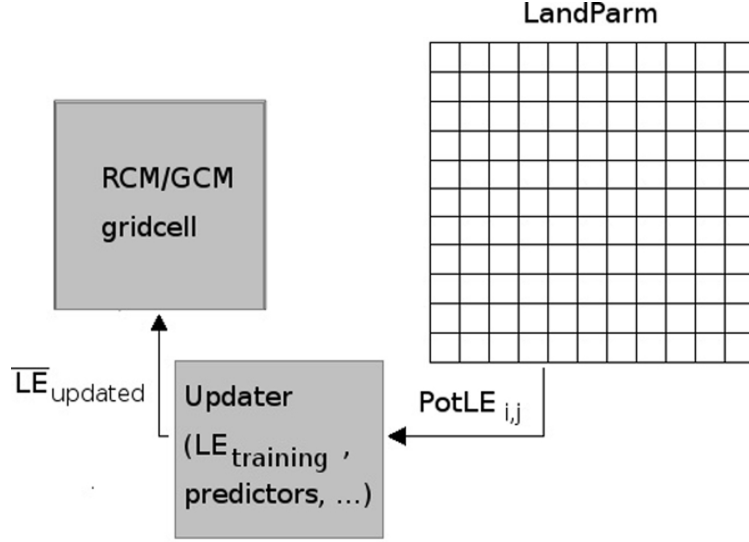


Figure 1. Scheme of the MCRA concept.

flow of water does not need to be simulated. This allows a reduction in the run time, that is estimated to be 1/15 of the standard run time for *CplxRun*.

The data for training the scheme are produced by a Complex Run (*CplxRun*), where the subsurface hydrodynamics is fully simulated and the water table is free to move.

We will develop a statistical model for the difference between *CplxRun* and *PotLERun* to function as the updater. Because *PotLERun* already includes much physics, the statistical model can be much more parsimonious than a full statistical model for the surface fluxes, and only focuses on correcting for the over abundance of soil moisture. Since the *PotLERun* does not provide a physically consistent water table depth, the topographic indices, that are proxies of the wetness of the soil, are used as predictors in the statistical model for the difference in evapotranspiration between the two runs, ΔLE .

The advantage offered by the use of simulations instead of measurements is the full availability of hourly data for the variables and full control on the

static parameters. The goal of this study is thus to develop a fast surface parameterisation that mimics LandCplx as well as possible.

For each class, the behaviour is assumed to be consistent and on average the same in the validation and in the training set. The predicted value for the latent heat, $LE_{pred,i}$, in each cell i of the class is calculated as the difference between the value of $LE_{pot,i}$ and the corresponding ΔLE , δ_i :

$$LE_{pred,i} = LE_{pot,i} - \delta_i \quad (1)$$

The value of δ_i is unknown during the prediction phase. It is approximated with the average ΔLE of the same class, as calculated in the training set, $\overline{\delta_{train}}$:

$$LE_{pred,i} = LE_{pot,i} - \overline{\delta_{train}} \quad (2)$$

In this way the error in the prediction for each cell is equal to the difference between the true value of ΔLE in the cell and the mean value of it for that class. The bias is then:

$$\overline{(LE_{pred,i} - LE_{true,i})} = \overline{(\delta_i - \overline{\delta_{train}})}, \quad (3)$$

meaning that if the residuals of the ΔLE values are homogeneously distributed, the bias will be small and the spatial mean of predicted latent heat will be a good approximation of the true value.

2.2 ParFlow.CLM

ParFlow is a variably saturated groundwater flow model with an integrated overland flow simulation capability. It has been coupled with *CLM* (Common Land Model) to incorporate physical processes that are related to the balances of energy and water at the land surface (*Maxwell and Miller, 2005, Kollet and*

256 *Maxwell*, 2006, 2008). *CLM* calculates the mass and energy balance at the land
 257 surface, in terms of evaporation from canopy and ground surface, transpiration
 258 from plants, ground heat flux, freeze-thaw processes and sensible heat fluxes.
 259 *ParFlow* replaces the soil column formulation and runoff scheme of *CLM*. The
 260 coupling between the two models is performed via soil moisture, evapotranspi-
 261 ration and infiltration of water. The atmospheric forcing can be represented by
 262 reanalysis data or the results from an atmospheric model.

263 **2.3 The simulations**

264 The analysis deals with the results of two *ParFlow.CLM* simulations (from now
 265 on, the *CplxRun* and the *PotLERun*) performed over a domain that includes
 266 the Rur catchment (*Rahman et al.*, 2014). The spatial resolution is $\Delta x = \Delta y =$
 267 1 km and the domain includes 168×168 cells. The soil is subdivided in layers,
 268 the thickness of which is increasing with depth (it varies from 0.04 m for the
 269 uppermost layer, to 4 m for the deepest one) in order to better resolve the
 270 dynamics in the shallow subsurface. The outputs consist of two-dimensional
 271 hourly data for the energy fluxes at the surface and three-dimensional hourly
 272 data for saturation and pressure in the subsurface, that span one year (namely
 273 2009). The water table depth is calculated based on the pressure profile in the
 274 subsurface, for each cell in the domain and each time step of the simulation.
 275 Positive values indicate cells where the groundwater table is below the surface,
 276 while negative values correspond to ponded water. The depth varies in time in
 277 response to the atmospheric forcing (*Rahman et al.*, 2014) and in space according
 278 to the hydraulic properties, gravity and pressure driven fluxes.

279 The domain encompasses a variety of land uses and soil textures (Figure 2).
 280 The land use classification follows the GLC2000 dataset (*Skalsky et al.*, 2009).
 281 The domain shows a large area of mostly natural vegetation in the southern

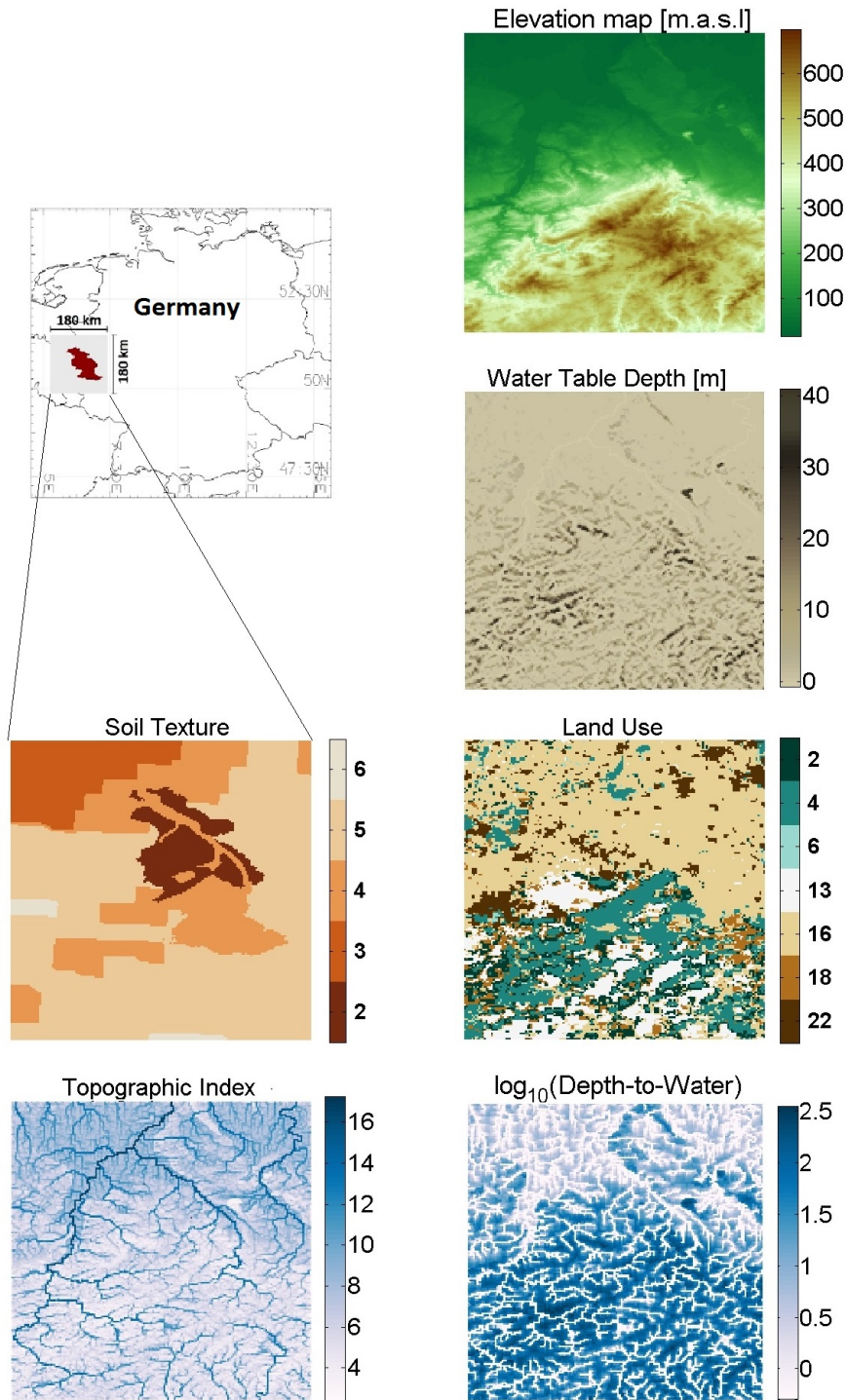


Figure 2. Overview of the topographic and surface characteristics of the domain. For the land use map, the correspondence is: 2) broadleaved deciduous trees; 4) needle-leaved evergreen trees; 6) mixed leaf type trees; 13) herbaceous cover; 16) cultivated and managed areas; 18) mosaic: cropland/shrub or grass cover; 22) artificial surfaces and associated areas. For the soil texture, the correspondence is: 2) silty clay; 3) loamy sand; 4) silt loam; 5) clay loam; 6) silt.

282 mountainous part, in correspondence to the Eifel National Park, while the north-
283 ern part is mostly covered by cultivated and managed areas. With regard to the
284 soil texture, silt is only present in two small areas, while clay loam represents
285 the most abundant soil type. Silt loam is present in both the mountainous and
286 the flat areas. Conversely, loamy sand is only present in the flat area. The Rur
287 catchment area mostly presents silty clay in the flat part and silt loam in the
288 mountains.

289 For the first simulation, the *CplxRun*, the subsurface hydrodynamics is al-
290 lowed to vary dynamically, in response to the spatial heterogeneity and the
291 atmospheric forcing. The setup for the second simulation, the *PotLERun*, only
292 differs from the *CplxRun* for the fact that the whole domain is kept close to
293 saturation by prescribing the pressure in the subsurface. The potential evap-
294 otranspiration is defined as “the rate at which evapotranspiration would occur
295 from a large area completely and uniformly covered with growing vegetation,
296 which has access to an unlimited supply of soil water” (*Dingman*, 2002). This
297 is the state which is simulated and which names the PotLERun. It represents
298 a measure of the demand of water from the atmosphere that the soil can fully
299 meet only if it is never water limited, as is the case in this simulation.

300 In this case the *CplxRun* represents the virtual truth, while the *PotLERun*
301 is Landparm, a numerically efficient parameterization providing insight on the
302 behaviour in case of extreme wetness.

303 The area is then split into a training and a validation subset. For the train-
304 ing set, both the results from *CplxRun* and *PotLERun* are used to develop the
305 statistical model. The model is then tested on the validation set, by correct-
306 ing the results of PotLERun, and comparing the corrected values against the
307 *CplxRun* results.

308 2.3.1 Statistical model

309 The diurnal cycle on one subset was fitted with a modified Gaussian function,

$$F(t) = A_0 + A * \exp\left[\frac{-(t - t_0)^2}{2 * w}\right] \quad (4)$$

310 using an offset A_0 , the difference between the maximum and minimum values
311 as height A , $t = 13$ as the central hour, t_0 , and a width, w , of 7 hours, for each
312 class of the topographic index. The parameters were estimated by means of a
313 dummy distribution with the same shape as the diurnal cycle over the month
314 of July (where the bell is more pronounced) and checked on the other months.

315 2.3.2 Validation method

316 In order to demonstrate the ability of the topographic indices to quantify the
317 ΔLE , the following procedure was applied. The entire domain was subdivided
318 into two subsets, one for the training and one for the validation of the method.
319 For the training data, the information coming from the *PotLERun* and the
320 characteristics of the cells (e.g., the topographic indices) were used as predictors
321 to develop a model for ΔLE . For validation, the outputs of the *CplxRun* were
322 used.

323 The two subsets are organized in a “checkers” scheme (Figure 3), where the
324 dark squares represent the training data and the whites are the validation, and
325 vice versa. To ensure independence, the size of the squares needs to be large
326 enough, thus the correlation length of the ΔLE was estimated. The analysis of
327 the variogram shows it to be no larger than 5 km, which means that squares of
328 21 km of side length are a reasonable choice.

329 The comparison against a free-drainage (*FD*) simulation (*Rahman et al.*,
330 2016) serves as a second method of validation. In the *FD* simulation, the mois-
331 ture is drained by gravity through the bottom of the domain, as opposed to



Figure 3. Training and Validation set 1 (left) and Training and Validation set 2 (right). The domain is subdivided into two subsets, according to a checkers scheme, that are used as training and validation set.

being redistributed in the subsurface according to the slopes. This boundary condition, commonly applied in land surface models, is known to have a “dry bias” due to the loss of water from the bottom of the column.

2.4 Topographic indices

2.4.1 Topographic Wetness Index

The *topographic index* (TI), also called *wetness index*, was introduced in 1979, in the framework of the TOPMODEL approach (Beven *et al.*, 1984, Beven and Kirkby, 1979). It is defined as

$$TI = \ln \left[\frac{\alpha}{\tan \beta} \right], \quad (5)$$

where the local slope β [-] is derived from the digital elevation model (DEM) and the specific catchment area α [m], is the area from which the water drains through the cell under investigation (contributing area), divided by the contour length. In equation 5, the slope determines the celerity of the runoff, while the contributing area is a measure of the potential amount of water. The TI represents an indicator of topographic heterogeneity in the catchment. It provides general information about shallow groundwater levels, at least in zones where

these are mainly determined by topography and, thus, may be an indicator of the availability of water for evapotranspiration. In the last decades, the topographic index has been widely used as an index of hydrological similarity, under the assumption that points of a catchment with the same value of TI behave similarly, from the hydrological point of view (*Beven, 1997*). In summary, the topographic index formulation is based on some general assumptions (*Beven, 1997, Ducharne, 2009, Franchini et al., 1996*) that are:

1. the local slope is a good approximation for the hydraulic gradient;
2. the dynamics of the water table can be approximated by a succession of steady states, in which an immediate balance between the local outflow from the saturated zone and the recharge from the contributing area is achieved at every time step and in every cell; and
3. the transmissivity of the soil declines exponentially with depth.

The validity of these assumptions varies between catchments and climates. If groundwater levels change slowly over time, for example, successive steady states represent the dynamics adequately (*Rinderer et al., 2014*).

Alternative and more complex indices have been proposed and used (*Hjerdt et al., 2004, Western et al., 1999*), such as the soil-topographic index (*Beven, 1986*) and the climato-topographic index (*Merot et al., 2003*), which include information about the transmissivity and the volume of annual effective rainfall, respectively. This is mainly necessary when a comparison between catchments with different characteristics, e.g., a different climatology, is performed or when the relaxation of some of the assumptions is necessary. For the purposes of this work the basic formulation is used.

The topographic index is computed from the slopes, with an algorithm that calculates the path of the water based on the maximum slope at every point and

counts the contributing cells for every pixel. The higher values of topographic index correspond with the river channels (cells that receive the largest contribution from the catchment), while low values of TI are characteristics of cells that receive small contributions in, e.g., headwater catchments.

2.4.2 Depth-to-Water Index

An alternative topographic index is represented by the Depth-to-Water (DTW) index. It is a measure of the difference in elevation between each cell and the closest river cell which it is most likely hydrologically connected to (*Murphy et al. (2009)*; *Rennó et al. (2008)* presents a different formulation, but an analogous concept).

Murphy et al. (2009) start from the DEM-derived slope and a flow-channel grid. An iterative function selects for every cell in the domain the nearest surface water cell and calculates the path that connects the two cells. This is then multiplied by the grid cell size, therefore approximating the total difference in elevation between each cell and the corresponding river cell. In this way, to each cell is assigned the value of

$$DTW = \left[\sum \frac{dz_i}{dx_i} a \right] x_c \quad (6)$$

where $\frac{dz}{dx}$ [-] is the local slope, i indicates the cell along the path, a is a coefficient that takes into account the direction of the flow across the cell (it is 1 when the flow is parallel to the grid lines and $\sqrt{2}$ when the flow is diagonal) and x_c [m] is the cell size (*Murphy et al., 2011*). The river network highly influences the values and the pattern of the index. Generally, the hydrographic information on the area are used to determine wheter a cell belongs to the river network or not.

Low values of DTW indicate the tendency to have water at or near the

surface, while drier areas have higher values, indicating a longer distance from the saturated areas (*Murphy et al.*, 2007). In the river channels, the *DTW* is zero by definition. Since the value assigned to each cell is the difference in elevation between that point and the associated river cell, the *DTW* index represents the elevation normalized with respect to the river network and corresponds to the relative position of the cell with respect to this datum.

The *DTW* index is also calculated from the slopes, with an algorithm that follows the flow of water (downslope) from each cell to the nearest (in the least cumulative slope sense) river cell. The value associated to each cell is the sum of the slope along the path, multiplied by the size of the cell, which yields the difference in elevation between them. In our implementation of the algorithm, only flow directions parallel to the cell borders are allowed (*D4*); the coefficient α is always 1. The cells are defined to be river cells according to a threshold in contributing area, which is also calculated based on the slopes. In order to ensure consistency, a comparison to the map of the rivers in the area and to the values of the average water table depth obtained from the simulation was performed. A threshold of 20 cells corresponding to 20 km² was found to be satisfactory.

3 Results and discussion

3.1 Exploratory analysis of data

In this section, the analysis of the results of the above mentioned simulations is presented, with a particular focus on the influence of soil composition and land use on the energy fluxes, and on the relation of the different variables with the topographic indices.

In the first part, the relationship between the latent heat flux and water

422 table depth is depicted. The two topographic indices, which will be used as
 423 predictors in the statistical model, are then briefly discussed and analyzed. For
 424 comparison, the relationship of latent heat flux with soil texture and land use
 425 are presented. Finally, the difference in latent heat flux between the two sets
 426 of simulations is analyzed, with respect to the predictors and other parameters,
 427 such as the land use and soil composition. The analyses focus mostly on the
 428 summer months and central hours of the day, since the difference in latent heat
 429 due to soil moisture limitations is expected to be largest in these times, in the
 430 study region (*Rahman et al.*, 2014).

431 **3.1.1 Relationship of the latent heat flux to the water table depth**

432 For the purpose of this analysis, the yearly average of water table depth is
 433 considered, in order to emphasize the relation to static parameters, such as the
 434 topographic indices.

435 Figure 4 shows the scatter plot of the monthly average latent heat flux (for
 436 the month of July) versus the water table depth, coloured according to land use
 437 (top) and soil texture (bottom). A typical pattern is present (see, e.g., *Szilagyi*
 438 *et al.* (2013); *Kollet and Maxwell* (2008)), where cells with a deep water table
 439 (over $\sim 5\text{m}$) show lower latent heat and cells with very shallow (under $\sim 1\text{m}$)
 440 water table have the highest values in latent heat. In these two extremes, the
 441 relation between latent heat and water table depth is weak, and small variations
 442 in water table depth do not influence the latent heat flux. Conversely, between
 443 these two extremes, the transition zone shows a steep relation between the two
 444 variables. This means that a small difference in water table depth results in a
 445 large variation in latent heat.

446 The month of July and the central hour of the day, 13.00, were chosen be-
 447 cause of their larger values of latent heat. In the winter months (October to
 448 March) there is no definition in the pattern and no S shape is visible. Dif-

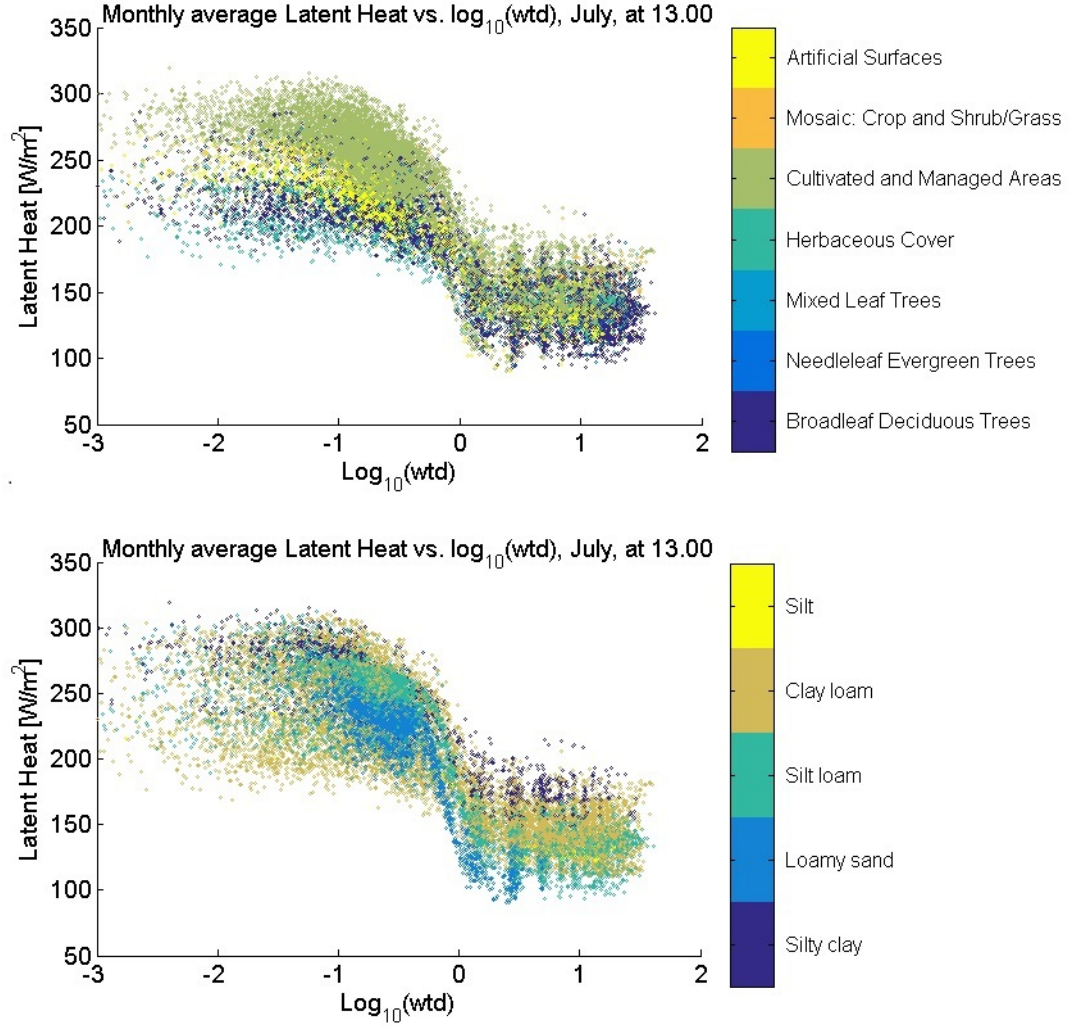


Figure 4. Scatter plot of the monthly average latent heat flux, for the month of July at 13.00, against logarithm of water table depth. The dots represent single cells in the domain and are coloured according to land use (top) and soil texture (bottom). Only cells with $wtd > 10^{-3}$ m are displayed.

449 ferent land uses and soil textures present different values of latent heat, e.g.,
 450 the herbaceous cover does not reach the high values shown by vegetation with
 451 higher leaf area index. With regard to the soil texture, the values of latent heat
 452 for silty clay mostly exceed those found for silt loam and loamy sand. While all
 453 these relations can be explained by the different hydraulic conductivities (for
 454 the soils) or root depths and leaf area indices (for the vegetation), the position
 455 of the cells in the domain also determines the availability of water, whose effect
 456 is superposed on the physical characteristics of the land cover and soil texture.

457 **3.1.2 Analysis of the topographic indices**

458 The Topographic Index for the domain is shown in Figure 2. The river channels
 459 correspond to the highest values of TI , but many other paths are visible, even
 460 where the water is not ponded over the surface, that correspond to the directions
 461 of the gravity driven water flow in the subsurface.

462 With respect to TI , which increases along the high flow accumulation ar-
 463 eas represented by the river channels and, more generally, by converging areas,
 464 forming narrow, discrete lines, the DTW index shows a smoother pattern (Fig-
 465 ure 2). In particular, DTW increases slowly in the flat northern part of the
 466 domain, while the increment is faster in the steeper terrain of the mountainous
 467 southern region.

468 The analysis of $\log_{10}(DTW)$ is useful to have a clearer image of the flatter
 469 area, where the index increase slowly with the distance from the river. For the
 470 similar, although inverted dependence on the slope, the $\log_{10}(DTW)$ shows a
 471 pattern similar to TI . In fact, there is a linear relationship between the two, as
 472 shown in Figure 5. The values are averaged using a moving average over squared
 473 neighbourhoods of 4×4 cells, as in *Murphy et al. (2011)*, in order to remove
 474 small-scale variability and get a clearer picture. The red line shows the linear
 475 fit, which has a coefficient of determination of ~ 0.81 . The inverse relationship

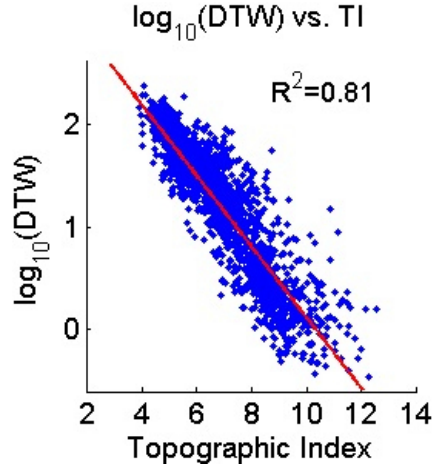


Figure 5. Scatterplot of $\log_{10}(DTW)$ and TI . The variables were previously averaged over 4 cells * 4 cells neighbourhood. The red line shows the linear fit, $\log_{10}(DTW) = -0.34 * TI + 3.57$.

between the two indices is due to their formulation: the topographic index accumulates the contributing area that is upslope with respect to the cell, while the DTW measures the distance (in height) between the cell and the closest river cell that is downslope. On the other hand, they both use the same algorithm for the determination of the path and both depend on the slope distribution of the catchment (but a logarithm is applied on the TI), which explains the close agreement between them.

3.1.3 Relationship between Latent Heat Flux and Topographic Indices

The topographic wetness index was developed to parameterize the water table depth, and therefore it is related to the soil moisture in the uppermost soil layers. Evapotranspiration is affected by the availability of water in the soil. The relation between water table depth and the land surface energy fluxes has been demonstrated in the past (*Kollet and Maxwell, 2008*) and also shown in Figure 4. For this reason we can expect to find a dependence of latent heat flux

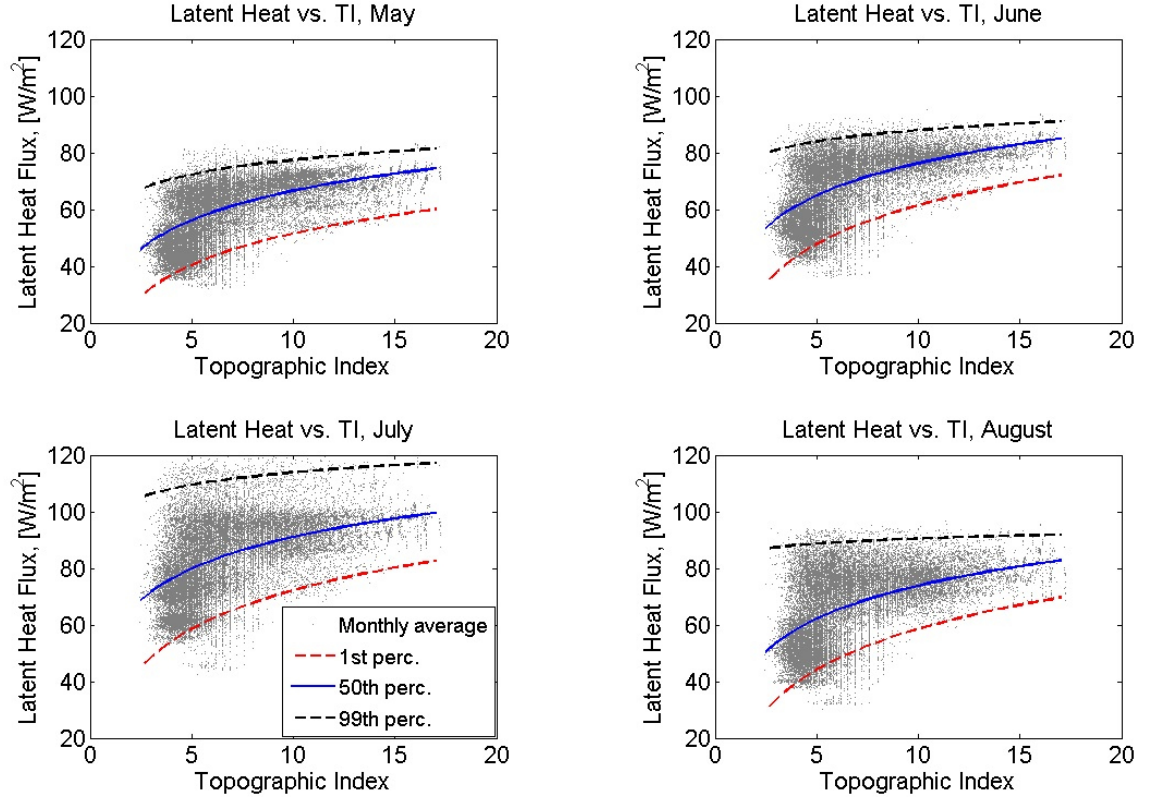


Figure 6. Scatter plot of the monthly average of latent heat against topographic index for the months from May to August. The lines represent the logarithmic fit of the 1st, 50th and 99th percentiles over small intervals of TI . Every cell in the domain is represented by its average value over the month.

491 on the topographic indices, as these are proxies for the water table depth.

492 Figure 6 show the scatter plots of the monthly average of latent heat flux
 493 and the topographic index, for every cell in the domain. Even if the values of
 494 latent heat flux show a large scatter for the same value of topographic index,
 495 a relationship can be found in the 1st, 50th and 99th percentiles, which were
 496 computed over TI bins of size 0.5.

497 While in winter (not shown here) the radiation is the limiting factor for
 498 the evapotranspiration, in summer this happens only for the cells that are not

499 limited in soil moisture. In the case of high topographic index ($TI > 12$), the
500 water table is shallow and there is full availability of water, that can fulfill the
501 atmospheric demand. The flat relationship between the latent heat and TI over
502 a certain threshold reflects the fact that the increment in soil moisture does not
503 automatically reflect into more evapotranspiration and is also consistent with
504 the relationship of latent heat to water table depth (see Figure 4). For low
505 values of topographic index, on the other hand, the water table is deeper, the
506 soil is not saturated and the system is water-limited.

507 Part of the scatter is due to the overlap of the effects of different kinds of
508 land use, as shown in Figure 7. Each colour corresponds to a different land
509 use class and every class is fitted using a first order Lowess technique, i.e. a
510 locally weighted regression method that reduces the influence of the outliers
511 by smoothing the curve and approximating the trend with local linear trends.
512 Every land use class presents similar trends, but for July the difference is much
513 larger than for the other months. For August, in particular, the water limitation
514 affected all the classes. It is also interesting to notice the different behaviour
515 of the herbaceous cover, which presents a lower latent heat flux, with respect
516 to the different categories of trees (broadleaved deciduous, needleleaf evergreen
517 and mixed leaf trees). Trees can produce higher evapotranspiration even in
518 areas with drier soil, corresponding to low values of topographic index. The
519 deeper root zone allows to reach deeper water tables and higher leaf area index
520 increases the transpiration.

521 The effect of the land use varies between months and is not always very
522 defined, because the resulting pattern is affected by other factors as well, for
523 example, the atmospheric forcings, such as radiation and precipitation, since
524 those vary within the domain.

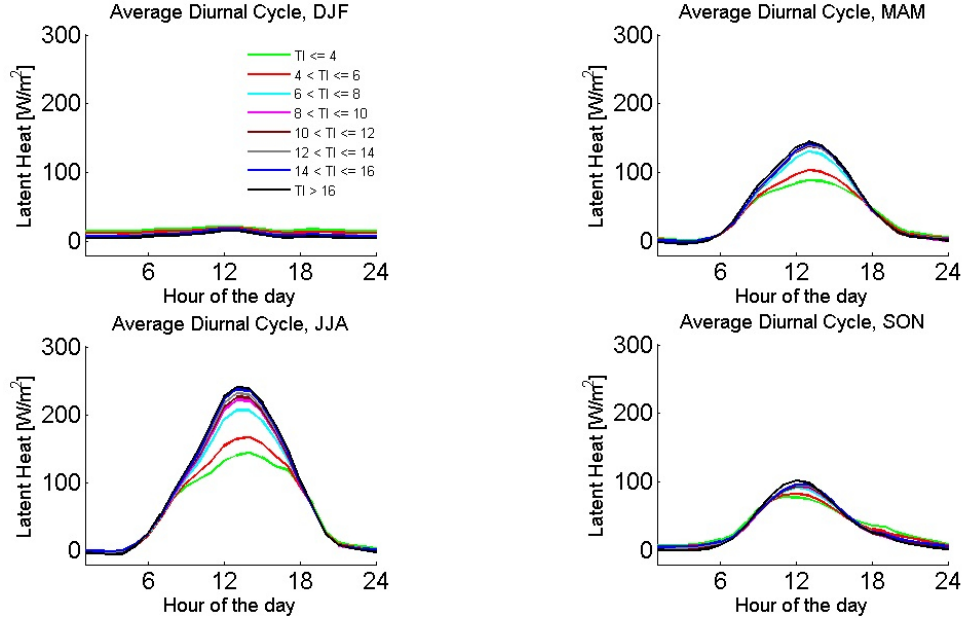


Figure 8. Overview of the seasonal average diurnal cycle of latent heat flux, for the different classes of TI .

3.1.4 Seasonal cycle of latent heat flux

Topographic index, as a measure of availability of water, is just one of the possible factors in determining the energy fluxes. Latent heat also has a diurnal and seasonal cycle, that reflects the availability of energy. Figure 8, shows the seasonal average diurnal cycle of latent heat flux for different classes of topographic index during the whole year. In order to obtain a smooth cycle and prevent spikes due to outliers, a 3-hour moving average was applied (see, e.g., *Deshpande and Goswami, 2014*).

The diurnal cycle shows higher values of latent heat for the summer months, in correspondence to the increased incoming radiation, as expected. Moreover, in these months the behaviour of the different classes of TI captures a larger variability, with maximum differences between the classes of TI of 50% around the middle of the day. This reflects the fact that neither energy nor water

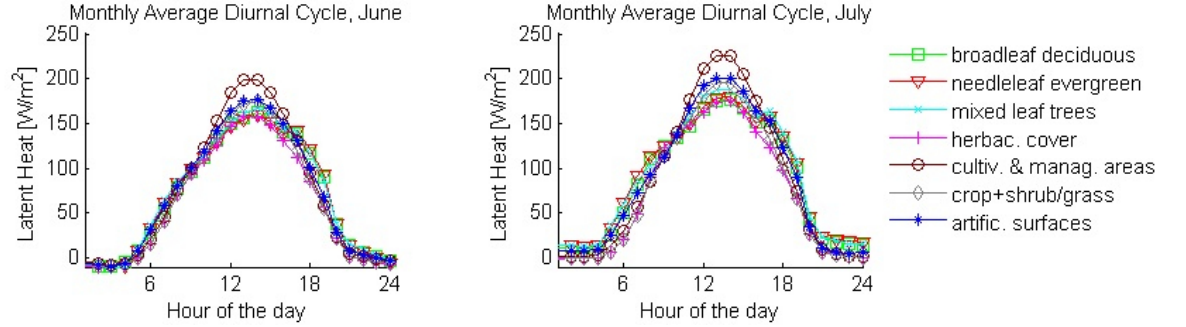


Figure 9. Monthly average diurnal cycle of latent heat flux for different classes of land use, for June and July. Every dot represents the average for one land use class and an hour of the day over the month.

are limited for cells with high TI in conditions of high incoming radiation, and is consistent with the larger dependence of LE on the groundwater during summer (*Rahman et al.*, 2014). During winter, on the other hand, the system is mostly energy-limited in this region of Germany and no real distinction is possible between the different classes of TI . For this reason we mostly focus on the summer months in our analysis.

It should be noted that the dependence on the topographic index does not only reflect a relationship to the hydrodynamics, since land use and soil are also partially correlated to topography (not shown) and are also key factors in LE .

3.1.5 Effect of land use and soil texture

As seen in Figures 6-7, the land use is also affecting the energy fluxes. It not only determines albedo, but is also central in the evapotranspiration processes. Figure 9 shows the diurnal cycle of latent heat for different kinds of land use, for two months. Land use is responsible for differences in the maximum (in the central hours of the day), but some variability is also present under conditions of very low incoming radiation, i.e. in the night hours, where the areas covered by trees show higher latent heat flux.

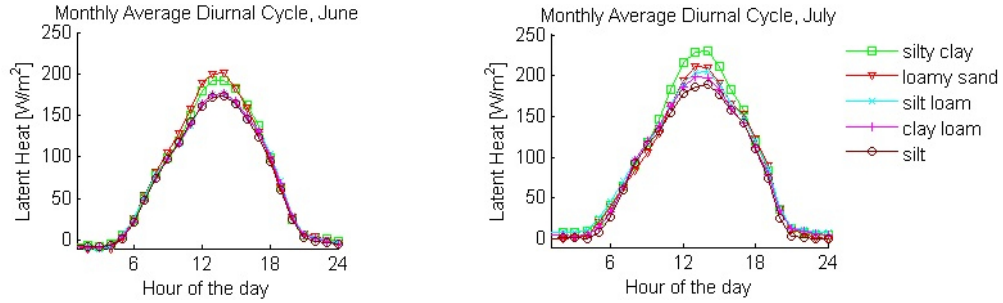


Figure 10. Monthly average diurnal cycle of latent heat flux for different classes of soil, June and July. Every dot represents the average for one soil type and an hour of the day over the month.

Figure 10 shows the monthly average diurnal cycle of latent heat flux filtered for the different soils for two months. The variability is less pronounced than for landuse, and is only present in the central hours of the day. Once again, it is important to notice that the effect of other variables, like landuse and topography, can be confounding factors.

3.1.6 Correlation of topographic index and latent heat flux

The main object of our analysis is the relationship between the topographic indices and the land surface processes and in particular the predictive skills of topographic indices with respect to the energy fluxes, also in comparison with other possible predictors (such as land use and soil texture). In the monthly average diurnal cycle (Figure 11), the topographic index TI shows a clear, direct correlation, i.e. higher values of topographic index correspond to higher values of LE flux for the central hours of the day and the difference between the maximum value for the highest and for the lowest class is larger than the difference between the classes of land use and between the classes of soil. The behaviour of the highest classes of topographic index do not show appreciable differences, since they are above the threshold in topographic index that corresponds to water tables at the surface, and so are virtually not water-limited.

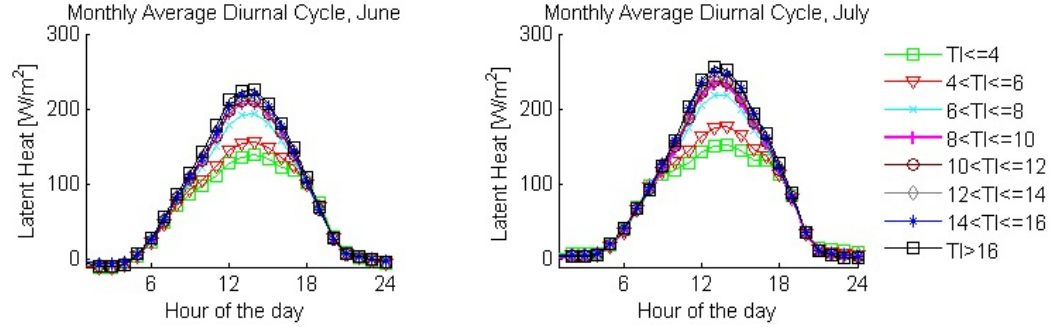


Figure 11. Monthly average diurnal cycle of latent heat flux for different classes of Topographic Index, June and July. Every dot represents the average for a class of TI and a hour of the day over the month. A 3 hour-moving average is applied.

573 This is in agreement with what was found previously in the scatter plots of
 574 the monthly average latent heat, but shows also a dependence on the hour of
 575 the day and a clear diurnal cycle for every class of TI , that was previously not
 576 visible. The monthly average diurnal cycles for classes of DTW (not shown)
 577 present an analogous pattern, with the classes corresponding to the highest
 578 availability of water having the highest LE .

579 3.1.7 Evapotranspiration surplus

580 In the case of the *PotLERun*, the water abundance in the cells does not depend
 581 on the TI , since the saturation is kept artificially at the surface. This means
 582 that useful information can be extracted from the comparison of the two runs,
 583 regarding the different behaviours of the cells in these two setups.

584 Figure 12 shows the map of the monthly average latent heat and potential
 585 latent heat, for July. While the potential latent heat mainly shows the signal of
 586 land use, with high values for the tree PFTs and lower values for the herbaceous
 587 cover, the latent heat in the *CplxRun* shows also the signal of topography (see
 588 Figure 2). For *PotLERun*, where the availability of water is kept artificially at
 589 its maximum, this signal is not present.

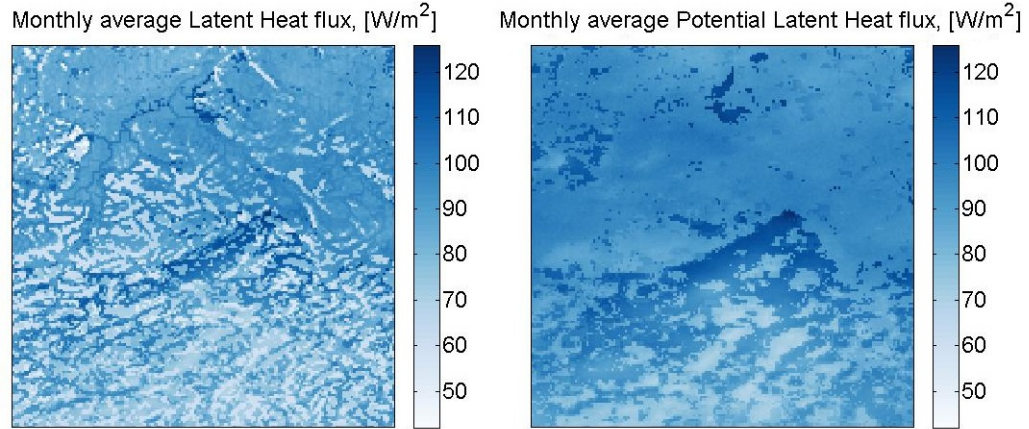


Figure 12. Map of the monthly average latent heat for the month of July, for the *CplzRun* (left) and for the *PotLERun* (right).

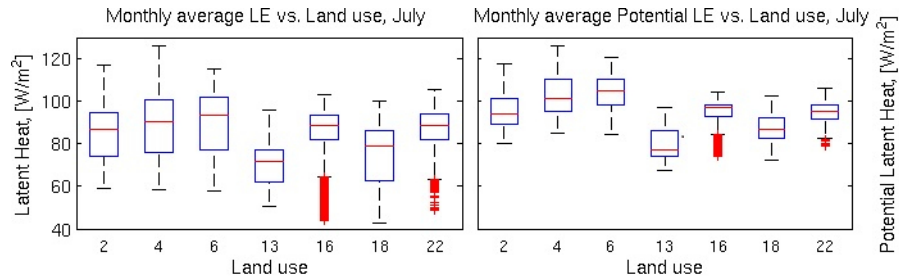


Figure 13. Box plots of the monthly average actual (left) and potential (right) latent heat flux (25th, 50th and 75th percentiles in the box, whiskers up to the most extreme non-outliers points and red crosses for the outliers) for different land uses, for the month of July. For the land use map, the correspondence is: 2) broadleaved deciduous trees; 4) needle-leaved evergreen trees; 6) mixed leaf type trees; 13) herbaceous cover; 16) cultivated and managed areas; 18) mosaic: cropland/shrub or grass cover; 22) artificial surfaces and associated areas.

Figure 13 shows the distributions of actual and potential latent heat flux for the month of July, for the different land use and soil type. In case of the potential latent heat, the first three boxes, that correspond to the tree cover, present the highest values, but this is less clear in the case of the actual latent heat, where the variability is larger because the availability of water also becomes an important factor. Moreover, the distributions are distinctly larger and the (ΔLE) values smaller for every land use in the actual latent heat, where the moisture limitation lowers the evapotranspiration in most of the cells.

We define *evapotranspiration surplus* the difference between the potential and the actual evapotranspiration in a cell, i.e. the evapotranspiration in the case of *CplxRun* and *PotLERun*, respectively.

Figure 14 shows the map of average ΔLE for the month of July. The signal of topographic index (Figure 2) is clearly visible. This is consistent with the fact that the only difference between the two runs is in the availability of water, which is strongly dependent on the topography in one case and kept constant in the other. Negative values of ΔLE , i.e., cells which present a monthly average potential latent heat lower than the actual latent heat, are rare but possible; the higher rate of evapotranspiration causes a drop in temperature that influences the evapotranspiration itself.

As already observed while analyzing the influence of TI on the latent heat, the evapotranspiration is strongly dependent on the availability of water. This is reflected in Figure 15, where the box plots of distributions of ΔLE for the different classes of TI are depicted. At high values of TI correspond no limitation in water and the evapotranspiration depends on the other parameters, first of all the energy. At low values of TI , on the other hand, the difference is larger. While the effect is clear for the median values, the spread of the distribution is large, in particular for the most populated classes of TI . The same dependence

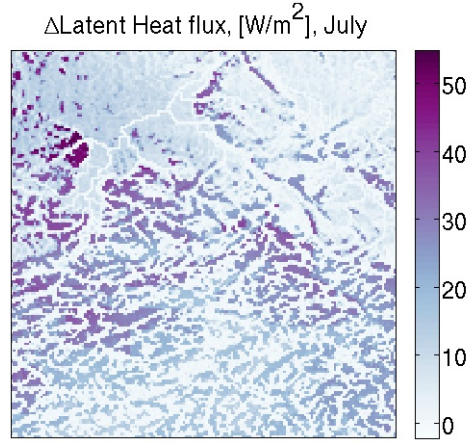


Figure 14. Map of the monthly average ΔLE for July, that clearly shows the signal of the topographic index.

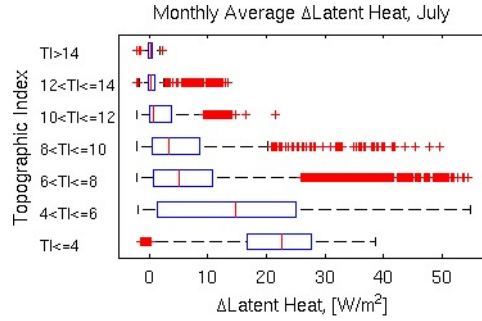


Figure 15. Box plots of the monthly average difference between potential and actual latent heat flux for different land uses, for the month of July.

617 of ΔLE on TI is present also in Figure 16, where the monthly average diurnal
 618 cycle of ΔLE for different classes of TI is shown. During the night, there is
 619 no visible difference between the TI classes. For the central hours of the day a
 620 clear dependence on the topographic index is visible. While for high values of
 621 TI the difference between the runs is close to zero, because the latent heat is at
 622 its potential, for low values of TI the difference becomes large, because in the
 623 *CplxRun* those cells are water-limited. The variability between the TI classes
 624 increases towards summer, with more classes exhibiting non-zero difference.

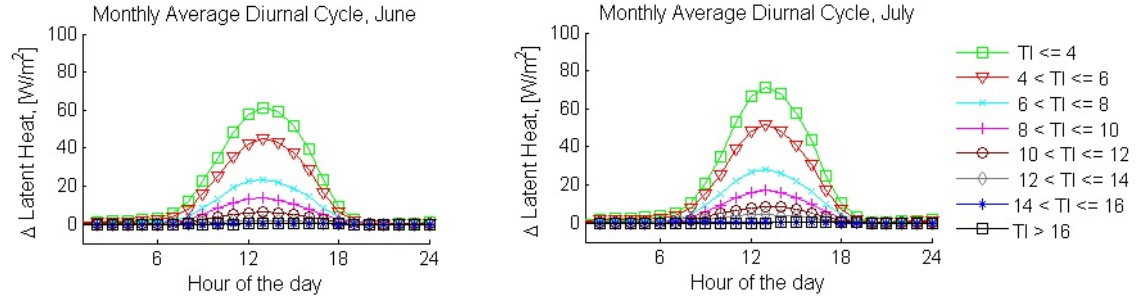


Figure 16. Monthly average diurnal cycle of ΔLE . The curves show the median value for each class of Topographic Wetness Index. A 3h-moving average is applied to the single hour values.

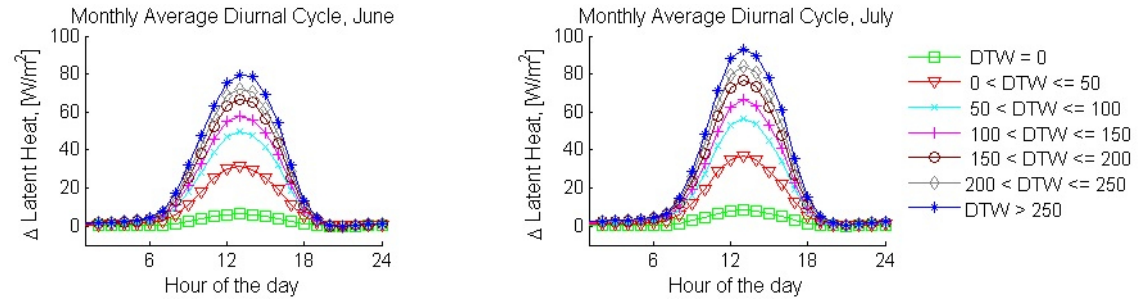


Figure 17. Monthly average diurnal cycle of ΔLE . The curves show the median value for each class of Depth-to-Water.

625 In Figure 17, the monthly average diurnal cycles for classes of DTW are
 626 depicted, for the months of June and July. As expected, and as already shown for
 627 TI , the increased availability of water in the classes with lower DTW is reflected
 628 in a smaller ΔLE . The difference is maximal when there is less limitation in the
 629 radiation (summer months, central hours of the day), while it is approximately
 630 zero during the night (or in the winter months, not shown here).

631 The shape of the diurnal cycle of ΔLE reflects the dependence on the in-
 632 coming radiation.

633 3.2 A model for latent heat flux

635 3.2.1 Validation method

636 In order to demonstrate the ability of the topographic indices to quantify the
637 ΔLE , the following procedure was applied. The entire domain was subdivided
638 into two subsets, one for the training and one for the validation of the method.
639 For the training data, the information coming from the *PotLERun* and the
640 characteristics of the cells (e.g., the topographic indices) were used as predictors
641 to develop a model for ΔLE . For validation, the outputs of the *CplxRun* were
642 used.

643 The two subsets are organized in a “checkers” scheme, where the dark squares
644 represent the training data and the whites are the validation, and vice versa.
645 To ensure independence, the size of the squares needs to be large enough, thus
646 the correlation length of the ΔLE was estimated. The analysis of the variogram
647 shows it to be no larger than 5 km, which means that squares of 21 km of side
648 length are a reasonable choice.

649 3.2.2 Statistical model

650 The diurnal cycle on one subset was fitted with a modified Gaussian function,

$$F(t) = A_0 + A * \exp\left[\frac{-(t - t_0)^2}{2 * w}\right] \quad (7)$$

651 using an offset A_0 , the difference between the maximum and minimum values
652 as height A , $t = 13$ as the central hour, t_0 , and a width, w , of 7 hours, for each
653 class of the topographic index. The parameters were estimated by means of a
654 dummy distribution with the same shape as the diurnal cycle over the month
655 of July (where the bell is more pronounced) and checked on the other months.

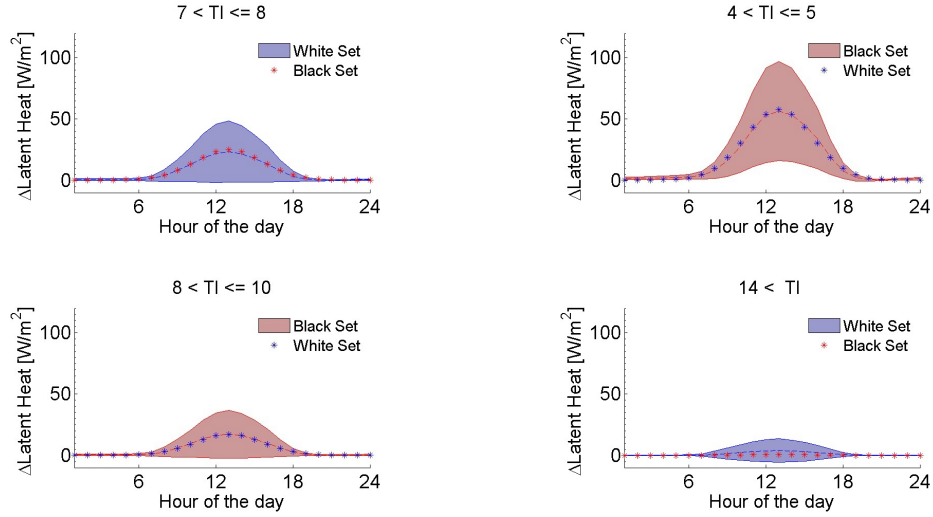


Figure 18. Examples of the comparison between the distribution of values of ΔLE for the black (white) subset of the domain -i.e. the validation subset- and the bell calculated on the white (black) subset for the same class of TI - i.e. the training subset. The dashed line represents the mean for the class and the filled area gives the standard deviation of the model. The stars show the values predicted for that hour and that class of TI , based on the corresponding data in the other subset.

3.2.3 Validation results

The plots in Figure 18 depict some examples of the monthly average diurnal cycles of ΔLE for a single class of TI . In order to represent the distribution of values, the mean (dashed line) and an interval of two standard deviations are displayed. The value predicted based on the information provided by the other subset are added for comparison (stars). In most of the cases, the function developed on one subset is able to reproduce the mean well in its counterpart, but some TI classes exhibit a large spread.

Similarly, in Figure 19 some examples of the monthly average diurnal cycles of ΔLE for single classes of DTW are depicted. As for the TI , also DTW is able to catch the average behaviour in each class fairly well, but the spread in

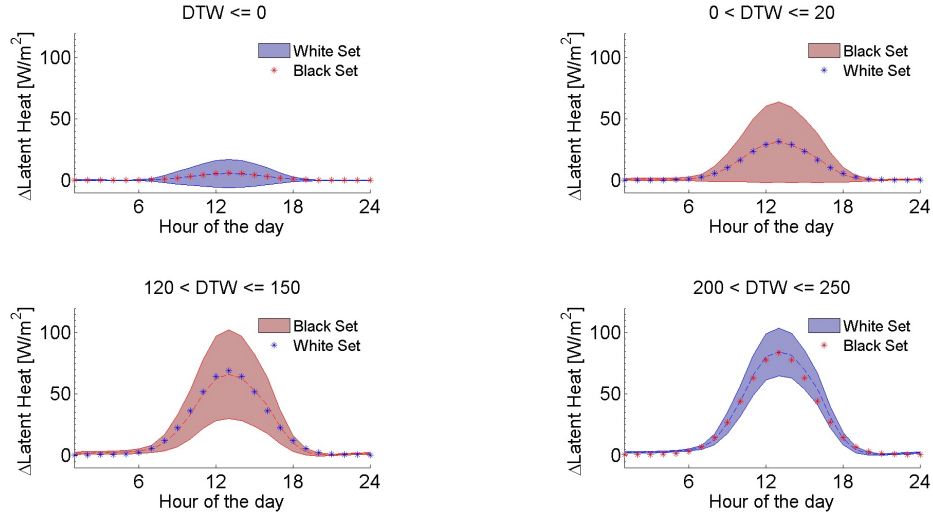


Figure 19. Examples of the comparison between the distribution of values of ΔLE for the validation subset and the bell calculated on the training subset. The dashed line represents the mean for the class and the filled area gives the standard deviation of the model. The stars show the values predicted for that hour and that class of DTW , based on the training subset.

the distributions is quite large.

When the value at the central hour is captured correctly, Equation 7 represents fairly well the values during the rest of the day. The central hour is also the timestep where the spread in the classes is largest. Figure 20 shows the map of the difference between the values of monthly average ΔLE predicted by the model and those simulated in the *CplxRun*, in the central hour of the day, for the model based on *TI* (left) and *DTW* (right). While the mean over the domain is close to zero in both cases, a clear pattern is present. Both negative and positive values are present (indicating, respectively, under- and overestimation of the latent heat flux), with mostly small scale structures in the southern part and a region with very high errors in both the models.

In order to study the origin of the larger scale structures in the bias, its relationship to the different landuses and soil composition was analyzed. In

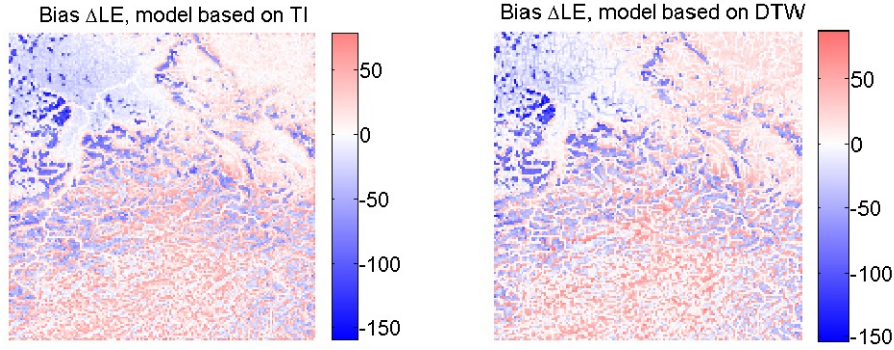


Figure 20. Maps of the difference between the monthly average values of ΔLE predicted and the values obtained from the simulation, for the central hour (13:00) of the day and the month of July. The prediction is based on TI and on DTW , respectively.

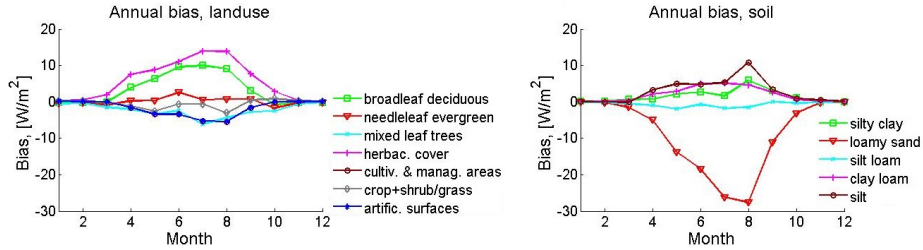


Figure 21. Plot of the mean bias of every class of landuse (left) and soil (right), for each month of the year at 13.00.

680 Figure21 , the annual trend of the prediction bias (based on TI) of the different
 681 classes is depicted, for both landuse and soil. While all the different landuses
 682 show comparable results, one of the soil types, loamy sand, presents a very high
 683 negative bias for the all summer months. This is in agreement with the large
 684 scale structure in the map of bias (Figure 20)

685 As an alternative form of validation, the results of the statistical model were
 686 tested against a free-drainage (FD) simulation (*Rahman et al.*, 2016). While
 687 this kind of land surface model is known to be a strong simplification, it still
 688 represents a widely used approach. The range of the error is equally large, yet
 689 the FD run shows a localized bias and poorly captures the spatial mean.

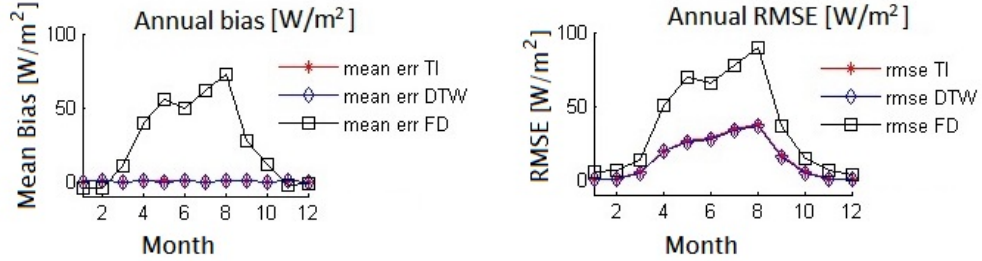


Figure 22. Comparison of the annual cycle of the root mean square error (left) and mean bias (right) for the free drainage simulation and the statistical models based on *TI* and *DTW*, at 13.00, for the monthly averages of *LE*.

690 The comparison of the root mean square error for the models (Figure 22)
691 shows similar performances for the two statistical models, and a better perfor-
692 mance compared to the free-drainage simulation. The choice of the central hour
693 of the day is meant to serve as a worst case scenario, since that is the condition
694 where the error is maximal. The fact that the bias is close to zero is a confir-
695 mation of the assumption that the mean ΔLE for the classes is representative
696 of the value for the single cells. This means that it is possible to predict the
697 values for areas where only the simplified model was run, based on the class of
698 topographic indices and the results of the full simulation in the training set, and
699 to obtain an accurate spatial mean that can be provided as boundary condition
700 to larger scale models.

701 4 Summary and conclusions

702 Groundwater is an important factor for the simulation of the energy fluxes at
703 the land surface. Unfortunately, a full-physics representation of the subsurface
704 hydrodynamics is mostly not feasible for climate simulations with long runs or
705 large domains. We propose an approach that reduces the computational burden,
706 by using a parameterized run and corrections based on the sensitivities of the

energy fluxes, and in particular of the latent heat flux, to topographic indices.

Two sets of simulations were used in the development of the model. The first simulation, *CplxRun*, is a full-physics simulation, the results of which represent the true values of the variables. The second simulation, Potential Latent Heat Run, *PotLERun*, is a highly parameterized version, where the water table depth is artificially kept close to saturation. This serves the purpose of saving computational time and shedding light on the behaviour of non water-limited cells, since the influence of the water availability is subtracted.

From the analysis of the results of the *CplxRun*, it is visible how the latent heat flux is strongly influenced by the availability of energy, as shown by the dependence on the time of the year and hour of the day, and by the availability of water. When the incoming radiation is not sufficient to trigger the evapotranspiration (in the winter months and in the night hours all over the seasons), the latent heat flux is close to zero and no evapotranspiration is present even for the *PotLERun*, despite the major water content in the soil. Even in the case of full availability of water, this does not translate into a systematic increase in evapotranspiration (Figure 6), since the energy is also a limiting factor.

Through the comparison of the latent heat in the *CplxRun* to its counterpart under conditions of full saturation (*PotLERun*), we were able to isolate the effect of the topographic indices and develop a statistical model to calculate the actual LE from the results of a parameterized run. The two topographic indices, the Topographic Index, TI , and Depth-To-Water, DTW , because of their relationship to the water table depth, are good proxies for the water availability, and show in general a significant effect on the diurnal cycle of latent heat flux, with respect to the land use and soil texture. The average diurnal cycles for the different classes of TI present a constant pattern over the year (Figure 8), where the high values of TI are related to the higher values of latent heat flux. While

the relationship between latent heat flux and topographic indices exhibits too much scatter to be able to establish a simple mathematical relationship with sufficient confidence, it was possible to develop a statistical model for the determination of the maximal value of the difference in evapotranspiration, ΔLE , corresponding to the central hour of the day, for each class of the predictor (TI or DTW). This value was then used to fit the top of the bell that represented the diurnal cycle.

The difference in latent heat between the two runs, evapotranspiration surplus (ΔLE) shows a marked relationship to the topographic indices (Figure 16), since everything is kept constant between the two simulations, except for the position of the water table. This means that the availability of water and all the quantities that derive from it, are well represented in the difference. The diurnal cycle of ΔLE for the classes of TI and DTW shows a bell shape, with the highest classes of TI and lowest classes of DTW presenting the lowest values of ΔLE (since they approximate their full potential in moisture).

The diurnal cycle for every class was then fitted with a modified Gaussian bell, that reproduces fairly well the diurnal cycle of ΔLE . While the mean values for each class are well behaved and are ordered according to the topographic index, the spread in some of the classes is very large. This is due to the fact that topography is not the only parameter influencing the surface energy fluxes. While part of the information about landuse and soil, for example, is present in the topographic indices, for the natural relationship between topography and surface characteristics, part of it is lost.

The validation of the method, through the extraction of two subsets and the comparison of the results obtained on the training subset to the distributions of value on the validation subset, showed a good agreement in the values of the mean. The domain was subdivided into two subdomains. Under the assumption

761 that the topographic indices are good predictors for the ΔLE , the bell fitted on
 762 the mean for each class of topographic index in one subset was superimposed
 763 to the distribution of the same classes on the second subset. The possibility of
 764 dividing the domain into two regions (east-west or north-south) was explored
 765 and had to be discarded. The major objection against the north-south sub-
 766 division was due to the deeply different average elevation, the southern area
 767 being mostly over 400 m.a.s.l. and the northern region being mostly flat and
 768 around 200 m.a.s.l., and the related different precipitation rate. For the east-
 769 west subdivision, the major concern was due to the different soil texture, and
 770 in particular with the loamy sand being only present on one side of the domain.
 771 The subdivision into two checkers subsets was able to capture the general trend
 772 and to avoid discrepancies due to large scale trends, but showed mixed results.
 773 While the model developed in the training subset was able to reproduce the
 774 mean in the validation subset very well, for some of the classes the spread was
 775 very large and this translated into large errors in the prediction of the ΔLE .

776 The two predictors, TI and DTW , do not show appreciable difference in the
 777 root mean square error and bias, but exhibit some differences in the spatial
 778 distribution. This is in agreement with the common basis of the two indices on
 779 the slopes. When compared against the free drainage run, results of a simulation
 780 where the soil moisture is allowed to leave the domain via gravity drainage,
 781 the statistical model performs satisfactorily, both in the winter and summer
 782 months. The low mean bias of the statistical model, in particular, indicates
 783 that the spatial mean of the predicted latent heat flux is a good approximation
 784 of the results provided by the full-physics model. In particular, the spatial mean
 785 could be provided to $GCMs$ or $RCMs$ as the lower boundary flux and would
 786 represent an improvement with respect to the free-drainage run.

787 Future work will substitute the discrete classes with continuous functions,

788 which will allow to reproduce the differences that are now neglected inside the
 789 classes and, in particular, the steep increment of latent heat flux for low values
 790 of topographic index TI . Further improvement may be achieved with an opti-
 791 mization of the fit of the diurnal cycle (e.g., via a machine learning approach for
 792 the estimation of the parameters over the different months). In an application,
 793 the *CplxRun* would only be used to model small catchments in a part of the full
 794 modelling area. Finally, an implementation of the concept over time should be
 795 explored, with a statistical model based also on the atmospheric forcing. This
 796 would allow to overcome the difficulties posed to the generalization of the results
 797 by the heterogeneity in soil and landuse.

798 References

- 799 Alley, W. M., R. W. Healy, J. W. LaBaugh, and T. E. Reilly, Flow and Storage
 800 in Groundwater Systems, *Science*, *296*, 2002.
- 801 Anyah, R. O., C. P. Weaver, G. Miguez-Macho, Y. Fan, and A. Robock, Incor-
 802 porating water table dynamics in climate modeling: 3 . Simulated groundwa-
 803 ter influence on coupled land-atmosphere variability, *Journal of Geophysical*
 804 *Research*, *113*, 1–15, 2008.
- 805 Betts, A. K., Understanding Hydrometeorology using Global Models, *Bull.*
 806 *Amer. Meteor. Soc.*, *85*, 1673–1688, 2004.
- 807 Beven, K., *Runoff Production and Flood Frequency in Catchments of Order*
 808 *n: An Alternative Approach*, pp. 107–131, Springer Netherlands, Dordrecht,
 809 1986.
- 810 Beven, K., TOPMODEL: A critique, *Hydrol. Process.*, *11*, 1069–1085, 1997.

811 Beven, K. J., and M. J. Kirkby, a physically based, variable contributing area
 812 model of basin hydrology, *Hydrological Sciences Bulletin*, 24, 1979.

813 Beven, K. J., M. J. Kirkby, N. Schofield, and A. F. Tagg, Testing a physically-
 814 based flood forecasting model (TOPMODEL) for three U.K. catchments,
 815 *Journal of Hydrology*, 69, 119–143, 1984.

816 Choi, H. I., and X.-Z. Liang, Improved terrestrial hydrologic representation in
 817 mesoscale land surface models, *Journal of Hydrometeorology*, 11, 797–809,
 818 2010.

819 Chou, C., and J. D. Neelin, Mechanisms of Global Warming Impacts on Regional
 820 Tropical Precipitation, *Journal of Climate*, 17, 2688–2701, 2004.

821 Decker, M., A. J. Pitman, and J. P. Evans, Groundwater Constraints on Simu-
 822 lated Transpiration Variability over Southeastern Australian, *Journal of Hy-*
 823 *drometeorology*, 14, 543–559, 2013.

824 Deshpande, N. R., and B. N. Goswami, Modulation of the diurnal cycle of
 825 rainfall over India by intraseasonal variations of Indian summer monsoon,
 826 *International Journal of Climatology*, 34, 793–807, 2014.

827 Dingman, S. L., *Physical Hydrology*, Upper Saddle River, NJ, Prentice Hall,
 828 2002.

829 Ducharne, A., Reducing scale dependence in TOPMODEL using a dimensionless
 830 topographic index, *Hydrology and Earth System Sciences*, 13, 2399–2412,
 831 2009.

832 Fan, Y., Groundwater in the Earth’s critical zone: Relevance to large-scale
 833 patterns and processes, *Water Resources Research*, 51, 3052–3069, 2015.

834 Fan, Y., and G. Miguez-Macho, Potential groundwater contribution to Amazon
 835 evapotranspiration, *Hydrol. Earth Syst. Sci.*, 14, 2039–2056, 2010.

836 Ferguson, I. M., and R. M. Maxwell, Role of groundwater in watershed response
837 and land surface feedbacks under climate change, *Water Resources Research*,
838 46, 1–15, 2010.

839 Franchini, M., J. Wendling, C. Obled, and E. Todini, Physical interpretation
840 and sensitivity analysis of the TOPMODEL, *J. Hydrol.*, 175, 1996.

841 Gleick, P. H., *Water In Crisis: a Guide to the World's Fresh Water Resources*,
842 New York: Oxford University Press, 1993.

843 Greve, P., B. Orlowsky, B. Mueller, J. Sheffield, M. Reichstein, and S. I. Senevi-
844 ratne, Global assessment of trends in wetting and drying over land, *Nature*
845 *Geoscience*, 7, 716–721, 2014.

846 Hjerdt, K. N., J. J. McDonnell, J. Seibert, and A. Rodhe, A new topographic
847 index to quantify downslope controls on local drainage, *Water Resources Re-*
848 *search*, 40, 1–6, 2004.

849 Jiang, X., G.-Y. Niu, and Z.-L. Yang, Impacts of vegetation and groundwa-
850 ter dynamics on warm season precipitation over the Central United States,
851 *Journal of Geophysical Research*, 114, 1–15, 2009.

852 Koirala, S., P. J.-F. Yeh, Y. Hirabayashi, S. Kanae, and T. Oki, Global-scale land
853 surface hydrologic modeling with the representation of water table dynamics,
854 *Journal of Geophysical Research*, 119, 75–89, 2014.

855 Kollet, S. J., and R. M. Maxwell, Integrated surface-groundwater flow modeling:
856 a free-surface overland flow boundary condition in a parallel groundwater flow
857 model, *Advances in Water Resources*, 29, 945–958, 2006.

858 Kollet, S. J., and R. M. Maxwell, Capturing the influence of groundwater dy-
859 namics on land surface processes using an integrated, distributed watershed
860 model, *Water Resources Research*, 44, 1–18, 2008.

- 861 Lam, A., D. Karssenberg, B. J. J. M. van den Hurk, and M. F. P. Bierkens,
 862 Spatial and temporal connections in groundwater contribution to evaporation,
 863 *Hydrol. Earth Syst. Sci.*, *15*, 2621–2630, 2011.
- 864 Leng, G., M. Huang, Q. Tang, H. Gao, and L. R. Leung, Modeling the effects
 865 of groundwater-fed irrigation on terrestrial hydrology over the conterminous
 866 United States, *Journal of Hydrometeorology*, *15*, 957–972, 2014.
- 867 Leung, L. R., M. Huang, Y. Qian, and X. Liang, Climate-soil-vegetation control
 868 on groundwater table dynamics and its feedbacks in a climate model, *Climate*
 869 *Dynamics*, *36*, 57–81, 2011.
- 870 Lo, M.-H., and J. S. Famiglietti, Effect of water table dynamics on land sur-
 871 face hydrologic memory, *Journal of Geophysical Research-Atmospheres*, *115*,
 872 2010.
- 873 Lo, M.-H., and J. S. Famiglietti, Precipitation response to land subsurface hy-
 874 drologic processes in atmospheric general circulation model simulations, *Jour-*
 875 *nal of Geophysical Research*, *116*, 2011.
- 876 Manners, J., J.-C. Thelen, J. Petch, P. Hill, and J. Edwards, Two fast radiative
 877 transfer methods to improve the temporal sampling of clouds in numerical
 878 weather prediction and climate models, *Quarterly Journal of the Royal Me-*
 879 *teorological Society*, *135*, 457–468, 2009.
- 880 Maxwell, R. M., and S. J. Kollet, Interdependence of Groundwater Dynamics
 881 and Land-Energy Feedbacks Under Climate Change, *Nature Geoscience*, *1*,
 882 2008.
- 883 Maxwell, R. M., and N. L. Miller, Development of a coupled land surface and
 884 groundwater model, *Journal of Hydrometeorology*, *6*, 233–247, 2005.

885 Maxwell, R. M., F. K. Chow, and S. J. Kollet, The groundwater–land–surface–
886 atmosphere connection: soil moisture effects on the atmospheric boundary
887 layer in fully-coupled simulations, *Advances in Water Resources*, *30*, 2447–
888 2466, 2007.

889 Merot, P., H. Quividant, P. Auresseau, M. Hefting, T. Burt, V. Maitre,
890 M. Kruk, A. Butturini, C. Thenail, and V. Viaud, Testing a climato-
891 topographic index for predicting wetlands distribution along an European
892 climate gradient, *Ecological Modelling*, *163*, 51–71, 2003.

893 Miguez-Macho, G., Y. Fan, C. P. Weaver, R. Walko, and A. Robock, Incorpor-
894 ating water table dynamics in climate modeling: 2. Formulation, validation,
895 and soil moisture simulation, *Journal of Geophysical Research*, *112*, 1–16,
896 2007.

897 Murphy, P. N. C., J. Ogilvie, K. Connor, and P. A. Arp, Mapping wetlands:
898 a comparison of two different approaches for New Brunswick, Canada, *Wet-*
899 *lands*, *27*, 846–854, 2007.

900 Murphy, P. N. C., J. Ogilvie, and P. Arp, Topographic modelling of soil moisture
901 conditions: a comparison and verification of two models, *European Journal*
902 *of Soil Science*, *60*, 94–109, 2009.

903 Murphy, P. N. C., J. Ogilvie, F.-R. Meng, B. White, J. S. Bhatti, and P. A.
904 Arp, Modelling and mapping topographic variations in forest soils at high
905 resolution: A case study, *Ecological Modelling*, *222*, 2314–2332, 2011.

906 Niu, G.-Y., Z.-L. Yang, R. E. Dickinson, L. E. Gulden, and H. Su, Development
907 of a simple groundwater model for use in climate models and evaluation with
908 Gravity Recovery and Climate Experiment data, *J. Geophys. Res.*, *112*, 2007.

909 Rahman, M., M. Sulis, and S. J. Kollet, The concept of dual-boundary forcing

910 in land surface-subsurface interactions of the terrestrial hydrologic and energy
911 cycles, *Water Resources Research*, *50*, 8531–8548, 2014.

912 Rahman, M., M. Sulis, and S. J. Kollet, Evaluating the dual-boundary forcing
913 concept in subsurface-land surface interactions of the hydrological cycle,
914 *Hydrological Processes*, *30*, 1563–1573, 2016.

915 Rennó, D. C., A. D. Nobre, L. A. Cuartas, J. Viane Soares, M. G. Hodnett,
916 J. Tomasella, and M. J. Waterloo, HAND, a new terrain descriptor using
917 SRTM-DEM: Mapping terra- firme rainforest environments in Amazonia, *Re-
918 mote Sensing of Environment*, *112*, 3469–3481, 2008.

919 Rinderer, M., H. J. van Meerveld, and J. Seibert, Topographic controls on
920 shallow groundwater levels in a steep, prealpine catchment: When are the
921 TWI assumptions valid?, *Water Resour. Res.*, *50*, 6067–6080, 2014.

922 Schomburg, A., V. Venema, F. Ament, and C. Simmer, Application of an adap-
923 tive radiative transfer scheme in a mesoscale numerical weather prediction
924 model, *Quarterly Journal of the Royal Meteorological Society*, *138*, 91–102,
925 2012.

926 Skalsky, R., Z. Tarasovicov, J. Balkovic, E. Schmid, M. Fuchs, E. Moltchanova,
927 G. Kindermann, and P. Scholtz, GEO-BENE global database for bio-physical
928 modeling v. 1.0, *Geobene Public Research Documents*, 2009.

929 Soyulu, M. E., E. Istanbuluoglu, J. D. Lenters, and T. Wang, Quantifying the
930 impact of groundwater depth on evapotranspiration in a semi-arid grassland
931 region, *Hydrology and Earth System Sciences*, *15*, 787–806, 2011.

932 Szilagyi, J., V. A. Zlotnik, and J. Jozsa, Net recharge vs. depth to groundwater
933 relationship in the Platte River Valley of Nebraska, United States., *Ground
934 Water*, *51*, 945–951, 2013.

- 935 Tian, W., X. Li, G.-D. Cheng, X.-S. Wang, and B. X. Hu, Coupling a ground-
 936 water model with a land surface model to improve water and energy cycle
 937 simulation, *Hydrol. Earth Syst. Sci.*, *16*, 4707–4723, 2012.
- 938 Venema, V., A. Schomburg, F. Ament, and C. Simmer, Two adaptive radia-
 939 tive transfer schemes for numerical weather prediction models, *Atmospheric*
 940 *Chemistry and Physics*, *7*, 5659–5674, 2007.
- 941 Vergnes, J.-P., B. Decharme, R. Alkama, E. Martin, F. Habets, and H. Dou-
 942 ville, A simple groundwater scheme for hydrological and climate applications:
 943 description and offline evaluation over France, *Journal of Hydrometeorology*,
 944 *13*, 1149–1171, 2012.
- 945 Vergnes, J.-P., B. Decharme, and F. Habets, Introduction of groundwater cap-
 946 illary rises using subgrid spatial variability of topography into the ISBA land
 947 surface model, *Journal of Geophysical Research: Atmospheres*, *119*, 11,065–
 948 11,086, 2014.
- 949 Western, A. W., R. B. Grayson, G. Blöschl, G. R. Willgoose, and T. A. McMa-
 950 hon, Observed spatial organization of soil moisture and its relation to terrain
 951 indices, *Water Resources Research*, *35*, 797–810, 1999.
- 952 Yeh, P. J.-F., and E. A. B. Eltahir, Representation of water table dynamics in
 953 a land surface scheme. Part I: Model development, *Journal of Climate*, *18*,
 954 1861–1880, 2005a.
- 955 Yeh, P. J.-F., and E. A. B. Eltahir, Representation of water table dynamics in
 956 a land surface scheme. Part II: Subgrid variability, *Journal of Climate*, *18*,
 957 1881–1901, 2005b.
- 958 York, J. P., M. Person, W. J. Gutowski, and T. C. Winter, Putting aquifers into

959 atmospheric simulation models: an example from the Mill Creek Watershed,
960 Northeastern Kansas, *Advances in Water Resources*, 25, 221–238, 2002.

961 Yuan, X., Z. Xie, J. Zheng, X. Tian, and Z. Yang, Effects of water table dynamics
962 on regional climate: A case study over east Asian monsoon area, *Journal of*
963 *Geophysical Research*, 113, 2008.